Effect of laser structured micro patterns on the polyvinyl butyral/oxide/steel interface stability

C.H.M. Hagen[a,*], O.Ø. Knudsen[b], A.H. Zavieh[c], W. Pfleging[d,e]

[a] *Department of Mechanical and Industrial Engineering, NTNU, 7491 Trondheim, Norway*
[b] *SINTEF, Richard Birkelandsvei 2B, 7465 Trondheim, Norway*
[c] *NTNU Nanolab, Sem Sælands vei 14, 7491 Trondheim, Norway*
[d] *Karlsruhe Institute of Technology, IAM-AWP, P.O. Box 3640, 76021 Karlsruhe, Germany*
[e] *Karlsruhe Nano Micro Facility, Hermann-von-Helmholtz-Platz 1, 76344 Eggenstein-Leopoldshafen, Germany*

ARTICLE INFO

ABSTRACT

This work investigated the effect of steel substrate topography and roughness on cathodic disbonding resistance and wet adhesion of the polyvinyl butyral/oxide/steel interface. Laser structuring was employed to pattern steel surfaces with controlled, periodic peaks of different peak-to-valley height, Rz, and geometry. Grinded smooth samples were used for reference. The in-situ scanning Kelvin probe technique was used to follow the cathodic disbonding in humid air and wet adhesion loss in inert atmosphere (3 ppm O_2). Both cathodic disbonding and wet adhesion loss depended on the ability of the surface for mechanical adhesion, even when compensating for the increased effective contact area. X-ray photoelectron spectroscopy excluded the possibility for oxide chemistry effects on the delamination rate. Surfaces with features that enabled mechanical interlocking forces, had the best cathodic disbonding resistance and wet adhesion properties.

1. Introduction

Conventional wisdom in the heavy-duty coating industry says that blast cleaning improves coating performance by enabling mechanical interlocking between coating and substrate, i.e. mechanical adhesion forces. The scientific community, on the other hand, has focused mostly on chemical bonds and intermolecular forces [1]. However, results from a recent study indicated that mechanical interlocking is vital for the performance of heavy duty protective coatings [2].

It is widely accepted that the resistance of an organic coating against propagation of electrochemical degradation is determined more by the steel/coating interface than its barrier properties [3]. The amount of oxygen and water present in organic coatings is normally sufficient to sustain a considerable corrosion rate [4,5]. Hence, the properties of the interface are critical, but still not fully understood. The standard explanation for the protective action of coatings, has been that coatings provide a high resistance between anodes and cathodes [6]. This work aims to study the effect of steel substrate topography and roughness on the stability of the coating/steel interface, measured as its wet adhesion property and resistance to cathodic disbonding (CD).

Various studies have addressed the role of roughness on the corrosion resistance of the coating/steel interface. However, all of them have

been performed on samples with non-uniform, heterogeneous topographies having a stochastic distribution of peak heights [7–13]. Most of the studies argue that the increased corrosion resistance is due to an increased effective contact area, as this will either offer more available area for bonds at the interface [14], or by increasing the interfacial path length and hence decrease the kinetics of failure [7,13]. Several studies have shown that coating/steel interfaces without mechanical interlocking, fail early when exposed to corrosive conditions [2,11,12]. Another study, although only covering a relative small range of roughness values (Ra of $0-1$ μm), argued that mechanical interlocking increased the stability of the coating/steel interface [10].

In this work, surfaces with periodic peaks of different peak-to-valley height and geometry were prepared by ultrafast laser structuring. Smooth samples prepared by grinding were used for reference. The composition of the bare steel surface oxide was characterized with X-ray photoelectron spectroscopy (XPS). Samples were coated with a model polyvinyl butyral-*co*-vinylalcohol-*co*-vinylacetate (PVB) coating [15–20], and 0.5 M NaCl electrolyte was added at a penetrative artificial defect in the coating. The potential of the coated surfaces was measured with the scanning Kelvin probe (SKP) technique as a function of exposure time in air and N_2 atmosphere.

The SKP technique has been established as an unique and powerful

---

method for non-destructive studies of the buried coating/metal interface [21–23]. It has mostly been employed for CD studies, but also for studies of wet adhesion properties of coatings by applying the technique in inert atmospheres [24]. The technique is able to map surface potentials through insulating layers of coatings as thick as 300 μm [25] with a typical lateral resolution of 100–150 μm [26].

CD proceeds from damages in organic coatings exposing the metal substrate and is believed to be the main de-adhesion mechanism on steels in humid and corrosive environments. The production of hydroxyls by the oxygen reduction reaction taking place underneath coatings, is balanced by migration of cations from the coating damage. The ingress of hydrated cations couples the intact steel-coating interface to external anodic sites, resulting in CD. The disbonding in air is driven by an electrochemical cell that comprises two separated galvanic half cells with anodic dissolution at the defect, coupled with the cathodic reduction of oxygen at the intact coating/oxide/steel interface. The progress follows parabolic kinetics, reflecting interfacial transport of ions as a rate determining step. The transport of hydrated ions at the coating/steel interface is a premise for the corrosion-induced degradation of organic coating-steel interfaces [22,27–31]. In inert atmosphere, the ingress of electrolyte from an artificial defect will not be controlled by an advancing corrosion cell but governed by the wet adhesion capability of the coating.

2. Experimental

2.1. Materials and samples preparation

The substrates were cold-rolled steel plates, EN 10130, with a chemical composition (in weight percent) of 0.04% C, 0.008% Si, 0.284% Mn, 0.0071% P, 0.0184% S, 0.033% Al, Fe to balance. The plates, with dimensions 30 mm × 60 mm and 4 mm in thickness, were grinded with SiC papers. Some were kept solely grinded, while the rest had 10 mm × 10 mm of the surface laser structured with ultrafast pulsed laser. See Table 2 for information about the surface structuring methods. The intention with the laser structuring was to create steel surfaces patterned with controlled 2D roughness profiles, representing different topographies with various roughness Rz. Ultrafast laser structuring enables high efficient material ablation without melt formation or heat impact to the surrounding material and offers the possibility of contactless rapid manufacturing of functional designs with high flexibility and process reliability [34,35]. It also allows for production of a uniform and homogenous surface texture. Before coating, all samples were thoroughly rinsed in ultrasonic bath with acetone and isopropanol and dried with an air blower. Samples were then stored in desiccators until the coating was applied. All grinded samples were exposed to ambient laboratory conditions (50–60% RH and $20-22\,°C$) for 2 days after grinding, before storage in desiccators. Studies performed by the authors and submitted for publishing, have shown that ongoing oxidation of the steel surface underneath the coating affects the coatings stability and cathodic disbonding resistance [36].

A polyvinyl butyral-*co*-vinylalcohol-*co*-vinylacetate (PVB) solution was prepared in isopropanol at 15.5% w/w PVB, by overnight stirring. Phenolphthalein was added at 6% w/w concentration for pH indication. Samples were coated using a draw-down bar. The PVB coating is a model coating often used for in-situ studies of the coating/steel interface stability [15–20]. The PVB coating cured for 6 days at ambient temperature inside a desiccator followed by 1 h in oven at 60 °C. The dry film thickness was 30 ± 5 μm above the peaks, measured with a magnetic coating thickness gauge.

Artificial defects were created by peeling the coating off the substrate to create a bare steel area of 10 mm × 10 mm metal in front of the laser structured area. The coating and defect preparation method was based on that of Stratmann et al. [4,37,38] and also used in other studies [15,18]. A sketch of the sample can be seen in Fig. 1.

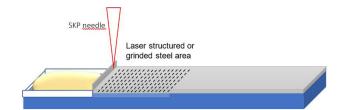All chemicals were obtained from Sigma-Aldrich and VWR.

Fig. 1. Sketch of the sample employed for evaluation of cathodic disbonding. A reservoir was created next to the area of interest, here indicated by the dashed lines. This was an area either uniformly micro patterned by laser, or grinded. The dimensions of the laser structured area were 10 × 10 mm. Electrolyte was added to the defect created according to Stratmann et al. [4,37,38], here seen at the left.

2.2. Laser structuring

Ultrafast laser-structuring was carried out on a micromachining workstation (PS450-TO, Optec, Belgium) equipped with a tunable fiber laser (Tangerine, Amplitude Systèmes, France).The maximum average power was 35 W and the maximum pulse energy was specified to 175 μJ at 1030 nm (TEM00 with $M^2 < 1.2$). The pulse repetition rate could be varied from single pulse to 2 MHz and the laser pulse duration from 380 fs to 10 ps, respectively. The laser beam was scanned over the sample surface for all experiments using a Rhothor™ Laser Deflection Systems scan head (Newson Engineering BV). All laser structuring processes were carried out under ambient air and the ablated material was removed by an exhaust. For details about the laser parameters, see Table 2.

2.3. Topography characterization

On the A surfaces, a non-contact Alicona optical Infinite-Focus Microscope (IFM) and a stylus profilometer was used to assess the ratio of effective contact area to geometrical area and the roughness Rz [33], respectively. Rz was measured by the profilometer according to the ISO 4287 definition.

On the laser structured surfaces, measurement of Rz and effective contact area were performed on cross-sections of minimum 2 samples, analysed with an Olympus GX51 optical microscope. The cross-sections were embedded in an acrylic resin, grinded with SiC papers (ANSI grade 80-320-500-1000-2400) and polished to mirror-like surface finish (water-based diamond suspensions with 3 μm followed by 1 μm particle size).

The regularity of the laser pattern was examined by scanning electron microscopy (SEM, Zeiss Ultra 55).

2.4. Chemical characterization of surfaces by XPS

X-ray photoelectron spectroscopy (XPS) was performed with an Ultra DLD Kratos system to study the composition of the various surfaces investigated in this work. Samples were analyzed immediately before the coating was applied, at two different positions, each of 0.7 × 0.3 mm, to ensure that the results represented the surface and not inclusions or certain defects at the surface. The pressure in the analysis chamber was kept below 5×10^{-10} Torr. Al Kα monochromatic source was used with emission current of 10 mA and 10 kV. The information depth was in the range of 3 nm. Spectra were calibrated using the carbon peak at 284.5 eV. The wide elemental scan was acquired for the wide energy range (0–1200 eV) with a pass energy of 160 eV and a step size of 1 eV. The high-resolution spectra were acquired with a pass energy of 20 eV and step size of 0.1 eV for precise energy position and peak shape determination.

CasaXPS was used for curve fitting, evaluation and quantification of the data. Shirley background subtraction was applied for peak deconvolution and fitting [39]. Full width half maximum (FWHM) was kept

constant for oxide components of each element and Gaussian/Lorentzian asymmetry was used for curve fitting using the parameters of standard peaks. Fe 2p 3/2 was used to investigate relative surface concentration of Fe_3O_4, FeO, Fe^{3+} (Fe_2O_3 and FeOOH) and metallic Fe. The splitting and peak position of metallic iron at 706.9 ± 0.2 eV and shifts in the oxides were in good agreement with reference peaks [40].

2.5. Scanning Kelvin probe measurements

In-situ SKP measurements were performed to investigate the effect of the steel substrate topography and roughness on the stability of the interface, measured as resistance to CD in air and ionic mobility in N_2 atmosphere. The SKP chamber was for the latter case flushed with nitrogen at RH 95% till 3 ppm oxygen concentration was measured. The stream of humid nitrogen through the $20 \times 20 \times 20$ cm^3 chamber was kept at 10 L/h.

All experiments were carried out at 25 °C and 95% RH, using 0.5 M non-deaerated aqueous NaCl in the defect reservoir. The NaCl employed in the experiments was from the same batch, i.e. the electrolyte was expected to contain the same oxygen concentration in all tests.

The SKP measurements were performed in a steel chamber, which both enabled accurate climatic control and acted as a Faraday cage.

The instrument was a Height-regulated SKP custom-made by Wicinski-Wicinski GbR. The theory behind the instrument has been covered by other works [4,21,37,38,41,42]. The probe was a 150 μm diameter NiCr needle, vibrating at 957 Hz with 5 μm amplitude above the sample surface accurately controlled by a double coil and permanent magnet displacement device. The working distance was approximately 60 μm. The resolution of the measurement depends on the needle diameter and the working distance, and was approximately 113 μm for this study [26]. The potential of the probe was calibrated in air against a Cu/CuSO$_4$ electrode (+0.320 V$_{SHE}$). All potentials are given relative to SHE. The SKP probe was scanned in steps of 40 μm over the coated surface along an 8 mm line normal to the defect-coating boundary and the profile lines, starting at this boundary. Minimum 2 parallel samples were tested for each condition. Several parallels were investigated simultaneously. The potentials of the bare steel surfaces employed in this study, were also measured with the SKP technique.

3. Results and discussion

3.1. Topography characterization

The laser patterning resulted in a series of equidistant and uniform linear peaks and grooves. Fig. 2 shows an example of a laser structured surface in plan-view, in this case the B2 surface. The profiles of all the surfaces are shown in Fig. 3. On the B, C and D surfaces the profiles differed in shape and height.

Tortuosity was calculated as the ratio of effective contact length to geometrical length across the surface profile according to Watts and Castle [7,13]. The ratios of effective contact area to geometrical area (Wenzel's roughness factor) were the same, since the profiles are straight in one dimension. Roughness and tortuosity are given in Table 2

3.2. Oxide characterization

The atomic concentration of the various iron oxidation states is shown in Fig. 4. The A surface had the highest concentration of metallic iron at the surface and the lowest concentration of Fe_2O_3/FeOOH. The oxides on the micro patterned samples were formed during the laser structuring. Within a surface layer of a few nm, a temperature rise in the order of 1000 K might be expected [43]. Together with the presence of oxygen, the process resulted in thermal oxidation of the steel surface. C surfaces had the highest concentration of Fe_3O_4 and Fe_2O_3/FeOOH at the surface.

Table 2 shows the Fe^{3+}/Fe^{2+} ratios for the surfaces. The C surfaces contained more trivalent iron than divalent. The increased presence of trivalent iron is not favorable to the oxygen reduction reaction due to reduced conductivity. However, a significant effect of the ratio on the electron transfer rate is seen first at a 10-fold increase in the ratio and higher [44,45]. The highest Fe^{3+}/Fe^{2+} ratio measured in this study was 1.26 on C surfaces, and the lowest was 0.80 on A surfaces. Hence, both the ratio and the variation between the surfaces were too small to affect the oxygen reduction reaction and the cathodic disbonding behavior. A difference of 60 mV was measured between the surface with the highest and lowest potential, which confirms that the electrochemical properties of the surfaces were quite similar. It has been shown before though that the surface composition affects not only the electron transfer rates during cathodic disbonding processes, and hence the CD rate, but may also affect adhesion forces [27,46]. A relationship between surface oxide chemistry and adhesion strength was demonstrated. The meaning of this is that it cannot be completely excluded that oxide chemistry may have contributed to the polyvinyl butyral/oxide/steel properties.

3.3. Coating/oxide/steel interface behavior in air and nitrogen atmosphere

The influence of steel topography and roughness on CD resistance and ionic mobility in inert atmosphere, the latter representing wet adhesion properties of the interface, were studied by SKP.

The CD results are shown in Fig. 5. CD in air proceeded with the typical sigmoid potential profiles as previously reported [15–20], characterized by two potential levels. The high potential plateau, corresponding to an intact coating/substrate interface, varied for the
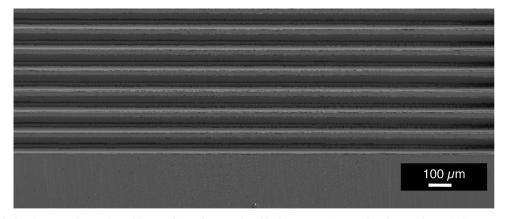

Fig. 2. SEM micrograph showing example top view of the equidistant lines produced by laser structuring steel surfaces with a periodic pattern of peaks. Sample B2 is shown here.
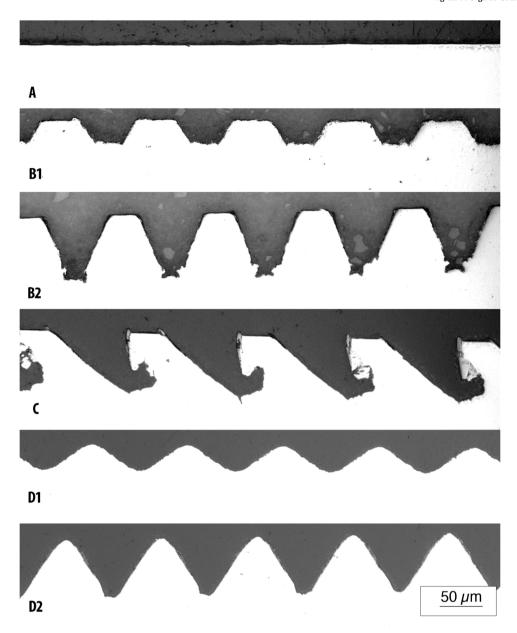
Fig. 3. Optical microscope images of cross-sections of the surfaces a) A, b) B1, c) B2, d) C, e) D1 and f) D2.

substrates in this study between 0.48 and 0.52 V_{SHE}. The potential of the intact interface is known to depend on the oxide composition [44], the applied coating [47], oxide/coating interactions [27,48] and the ingress of humidity and gasses [49]. Since the oxide composition was rather similar for all the surface profiles tested (see Fig. 4), and the test conditions were the same, the small variations in this potential between the various surfaces was expected.

The low potential area close to the defect is attributed to the area with disbonded coating. Potentials of -0.1 to $-0.2\,V_{SHE}$ were measured close to the defect, which correlates well with previous studies [50].

The CD front, or the "electrolyte front position" [41], has been defined as the position of largest potential change between these two areas [4,37,38]. The NaCl electrolyte at the defect feeds the interface with hydrated cations. Once an electrolytic contact is established with the intact interface, the potential at the respective position is cathodically shifted towards the anodic defect potential. The potential of corroding steel in 0.5 M NaCl is typically -0.3 to $-0.4\,V_{SHE}$ [42]. The electrolytic contact of the intact interface with the coating defect,

allows the oxygen reduction reaction to occur underneath the coating without the kinetical inhibition that an intact interface represents [51]. The disbonding front position is hence located at the transition from areas where the oxygen reduction reaction is kinetically free to happen, to areas where it is hindered. The location of this front is seen at the inflection point in the sigmoid potential profile, and its lateral shift is commonly used as a sign for the propagation of the CD process.

The potentials close to the defect on B2 and D2 surfaces decreased to $-0.1\,V_{SHE}$ during the first $3-4\,h$ of the test, before increasing to about $0\,V_{SHE}$ towards the end of the test. On C surfaces, the potential close to the defect never decreased beyond $0\,V_{SHE}$, and during the test the potential increased to about $0.2\,V_{SHE}$. In all cases the potential profiles were sigmoid shaped, typical for the CD process. Considering all the six types of surfaces, the final potential at the defect correlates to some degree with the CD distance. Samples with little disbonding had higher final potential near the defect. A potential increase on bare steel can be caused by passivation. Wielant et al. [27] explained deceleration of CD propagation with passivation of the defect. The driving force for the CD is then decreased as the defect potential is increased [38,51].
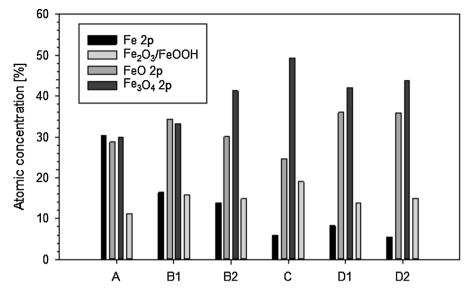
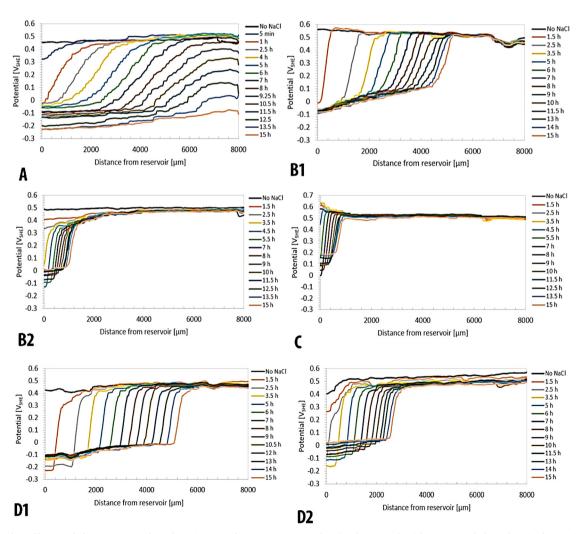**Fig. 4.** The amount of iron species measured by XPS on the surfaces.

Fig. 5. Potential profile recorded on PVB coated steel in air atmosphere at 95% RH and 25 °C, during 15 h with 0.5 M NaCl electrolyte in the coating defect. The potential profiles were recorded on a) A surfaces, b) B1 surfaces, c) B2 surfaces, d) C surfaces, e) D1 surfaces and f) D2 surfaces.

The CD resistance on B2, C and D2 was indeed higher than on the other samples. However, an increasing defect potential is not explaining the large effect of surface roughness on CD. The effect has also been found with cathodically polarized samples, where the defect potential was constant [11].

The phenolphthalein indicator in the PVB coating showed that an alkaline environment developed under the coating, initially close to the defect and propagating with time. The violet phenolphthalein chromophore is at its strongest at pH 10, hence the color that developed implied that the local pH underneath the disbonded coating was at 10 [52]. The color front followed in all cases the disbonding front identified from potential profiles. The color change propagation during the test was not accurately measured, but after the test the color front was found to be identical to the location of the potential increase.

On A surfaces, the potential above *the intact* coating/oxide/steel interface was seen to decrease after about 8 h. Potential decreases above intact coating/steel interfaces, are usually related to a weakening of bonds [49] and activation of the metal surface. Hence, the coating also failed by a second degradation mechanism, probably a general adhesion loss due to hydrolysis of adhesive bonds caused by water absorbed in the film. On A surfaces the PVB coating had disbonded completely, allowing the electrolyte to leak through the coating.

After the test, the disbonded PVB coating was removed on all samples. After 15 h, the trend for the measured disbonded length was A > D1 > B1 > D2 > B2 > C.

Despite the cathodic disbonding process identified in the potential profile scans, and the phenolphthalein pH indicator color shift in the coating close to the defect, the coating still adhered strongly to the B2 and C surfaces in the areas with CD. On the D2 surfaces, post-test adhesion in the disbonded area varied between parallels. These observations are probably explained by mechanical interlocking with the surface profile of the substrate.

The wet adhesion loss observed on the A surfaces was further studied on all the surfaces in an oxygen deficient atmosphere. Wapner et al. found that the ingression of electrolyte along the interface from a defect measured in inert gas, may result in wet de-adhesion [24]. If the potential in the vicinity of the defect does not return to values corresponding to the pristine coating/steel interface (see Fig. 5), when changing from inert air to oxygen atmosphere, a de-adhesion of the coating happened with the incorporation of hydrated ions along the interface in inert atmosphere.

The oxygen concentration was kept at 3 ppm with the exception for $3-5$ min when the chamber door was opened and oxygen containing air then entered, first when the samples were introduced, and later when the NaCl electrolyte was added in the defect. The oxygen content temporarily increased, but after 5 min the 3 ppm oxygen concentration was reached upon new nitrogen purging. Surfaces were kept in the humid nitrogen atmosphere for up to 45.5 h, see Fig. 6.

The A surfaces without the ability for mechanical interactions experienced decreased adhesion even in the absence of oxygen, and the coating could be peeled-off at the end of the test. The samples seem to have suffered from a hydrolytic induced destabilization of adhesive bonds. Previously it has been suggested that water reaching the interface may more readily result in bond breaking [53] on such surfaces. Beside breaking of secondary bonds by hydrolysis, a mechanical breaking of bonds has also been proposed [54]. When in addition structural changes take place at the interface due to swelling of the coating, adhesive bonds may be broken [27].

The potential profiles confirm otherwise results from previous studies, showing that ionic mobility in oxygen deficient atmosphere mirrors the ionic mobility in air but happens at lower rates [28,29]. The length over which ions were found to have entered, was smaller compared to the length measured in air, but in general the same trend as seen from potentials scans in air were found. B2 and C, followed by D2 surfaces again display an interface that most efficiently resists the ingress of ions. The ingress of sodium ions at the interface is believed to be migration driven by the hydroxyl production either from the hydrogen reduction reaction [55] or from the reduction of small amounts oxygen trapped at the oxide surface [28,29], or to be a pure diffusive process [24].

3.4. The effect of topography on CD rate

It is found that CD is inversely proportional to tortuosity, see Fig. 7. The relationship presented here on surfaces patterned with a uniform and homogeneous surface texture, confirms thereby results from a previous study on heterogeneous surfaces with different blast cleaning profiles [7]. It was then concluded that roughness affects the cathodic disbonding resistance by the increased interfacial path length for ionic transport, although the study covered a relatively small population of interfacial area (tortuosity measured at 1–1.12). The number of bonds broken by CD should therefore scale with increased contact length at
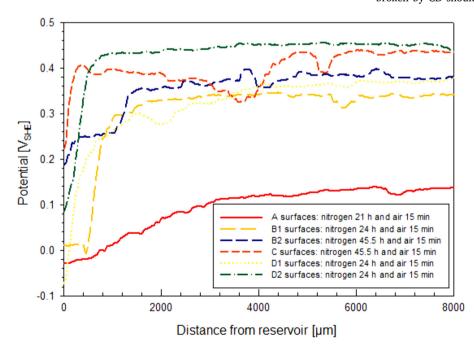

Fig. 6. SKP potential scanning of the ionic mobility in oxygen deficient atmosphere ($O_2 = 3$ ppm) at 95% RH and 25 °C, with 0.5 M NaCl as defect electrolyte. The potential profiles on A, B1, D1 and D2 were scanned after 21–24 h of nitrogen and 15 min with air. B2 and C surfaces were taken after 45.5 h of nitrogen and 15 min with air.
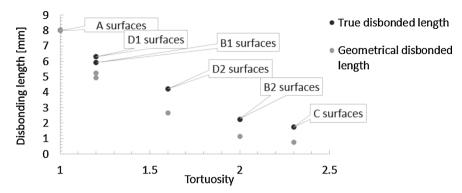
Fig. 7. The disbonded length, as it was measured and as it was calculated as a function of tortuosity, i.e. the ratio between effective interfacial length and geometrical length.

Table 1

Nomenclature. Roughness parameters according to ISO 4287 [32] and ISO 4288 [33].

Parameter	Description	Mathematical definition
A	Actual surface profile area. The effective contact area.	
A_0	Geometrical area	
L	Actual surface profile length. The effective contact length.	
L_0	Geometrical length	
Rz	Average maximum peak to valley distance for five sampling lengths within the measurement length l	$Rz = \frac{1}{5} \sum_{i=1}^{5} (Rp + Rv)_i$ Rp is the largest profile peak height and Rv the maximum profile valley depth within one of the five sampling lengths of the measurement length l.
Tortuosity	Ratio between actual surface profile length to geometrical length	$T = L/L_0$
Wenzel's roughness factor	Ratio between actual surface profile area to geometrical area	$W = A/A_0$

Table 2

Surface conditions, structuring method and roughness of the steel samples used in the study. The Fe^{3+}/Fe^{2+} ratio calculated from the amount of iron species measured by XPS on the surfaces and the potentials [V_{SHE}] measured on uncoated surfaces at 95% RH and 25 °C measured by the SKP.

Surface	Structuring method	Roughness Rz [μm]	Tortuosity	Surface potential [V_{SHE}]	Fe^{3+}/Fe^{2+} ratio
A	Abrasive grinding 80-320-500-1000 grit (ANSI) SiC papers	0.40 ± 0.01	1.01 ± 0.10	0.47 ± 0.01	0.80
B1	Wavelength: 1030 nm Power: 4.05 W Repetition rate: 400 kHz Scan speed: 400 mm/s	25.0 ± 0.10	1.21 ± 0.01	0.50 ± 0.00	0.84
B2	Hatch distance: 10 μm Laser pulse length: 380 fs Number of repetitions: 20 (B1), 50 (B2)	64.1 ± 0.10	1.99 ± 0.05	0.50 ± 0.00	0.97
C	Tilt angle (Sample – working stage): 30° Wavelength: 1030 nm Average laser power: 2 W Laser repetition rate: 400 kHz Scanning speed: 2 m/s Hatch distance: 5μm Pulse duration: 380 fs Number of repetitions: 120	58.4 ± 3.80	2.31 ± 0.1	0.52 ± 0.02	1.26
D1	Wavelength: 1030 nm Average laser power: 1.22 W Laser repetition rate: 400 kHz Scanning speed: 2 m/s	28.0 ± 0.70	1.17 ± 0.04	0.48 ± 0.02	0.84
D2	Hatch distance: 5μm Laser pulse length: 380 fs Number of repetitions: 8 ablation lines with varying rep. numbers	60.7 ± 0.20	1.61 ± 0.01	0.53 ± 0.03	0.87

the interface, such that same disbonded length would be measured on rough surfaces as on smooth surfaces, after a given time. Disbonded length multiplied with tortuosity should be constant for the various profiles tested. However, in this study we found a decay.

Fig. 7 shows the disbonded length as it was measured geometrically after 15 h, and the true disbonded length when geometrical length is multiplied with the tortuosity (see Tables 1 and 2), and plotted against tortuosity. The plot shows a decay. Using least-squares regression, different trendlines can be fitted to the data set. An exponential inverse relationship was found with an $R^2 > 0.99$ for both series. The relative standard deviation for the disbonding lengths measured after 15 hours, was calculated for two parallel samples treated and tested according to the same scheme, and found to be 18% for B2, 13% for C and < 4% for the other surfaces.

In the mechanistic studies of CD on iron and steel, the disbonding has often been found to be proportional to the square root of time,
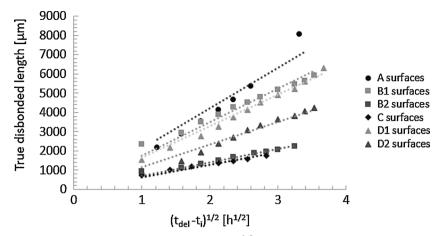
Fig. 8. Plots of true CD distance measured in air atmosphere as a function of $(t_{del} - t_i)^{1/2}$ at 25 °C for a 30 μm PVB coating on steel with different peak patterns and roughness Rz. The electrolyte at the defect is 0.5 M NaCl (aq).

indicating that the transport of hydrated ions at the coating/substrate interface determines the CD rate [3]. This has been reported both for PVB [56] and epoxy coatings [57–59]. The disbonded distance is then related to the time of electrolytic contact (t_{del}) and an initiation time, (t_i), by Eq. (1) [56]

$$X_{del} = k_{del}\sqrt{(t_{del} - t_i)} \tag{1}$$

k_{del} is the disbonding rate constant. In Fig. 8, the term X_{del} in Eq. (1) has been corrected to the true interfacial disbonded length and plotted as a function of $(t_{del} - t_i)^{1/2}$. The initiation time for CD is understood as the time needed for diffusion of water and oxygen into the coating and establishment of the galvanic cell [60,61]. The initiation time was found to be similar on A, B1, D1 and D2, while it was twice as high on B2 and three times as high on C, with 4.5 h and 7 h respectively. The curves are straight lines, consistent with a rate control by cation migration. The slopes of the lines, corresponding to the k_{del} term in Eq. (1), confirms the trend for CD seen in potential profile plots in Fig. 5. On smooth A surfaces, the CD advances much faster than on C surfaces patterned with tilted and curved peaks, even when compensating for the increased effective contact area. Increased effective contact area therefore cannot explain the increased CD resistance alone. Mechanical interlocking is probably the explanation.

In theory, mechanical adhesion will decrease lifting of the disbonded coating, narrowing the gap between the disbonded coating and the substrate. Hence, the cross-sectional area for cation migration between the coating defect and the CD front will decrease, increasing the ohmic resistance. The potential drop in this area, is explained to be an ohmic potential drop according to Eq. (2) where i_{galv} is the interfacial current density approximated by i_c, the interfacial cation current density. And R is the ohmic resistance in the electrolyte against interfacial cation transport

$$\Delta U_\Omega = i_{galv} \times R_\Omega(x) \tag{2}$$

A narrower gap at the interface, would increase the potential drop between the defect and the CD front, i.e. an increased potential profile underneath the disbonded coating. The potential profiles for D1 and D2 surfaces in Fig. 5, however, do not seem to differ. In fact, except for B1, all the surfaces have rather flat potential profiles between the coating damage and the CD front.

The quantification of the interfacial cation current density and the electrolytic resistance is difficult. A reduced potential drop will however result from an increased resistance accompanied by a decreased galvanic current. This implies a decreased cationic mobility rate at the interface. Obvious reasons for such a decrease may be explained with increased interfacial transport path for the ions. The surface asperities increased the effective contact area on the surfaces studied here. In

addition, the asperities develop friction forces at the interface, i.e. between the coating and the substrate. The friction forces depend on the specific structure and height of the asperities. See Fig. 9.

The balance of friction forces acting at the interface will determine the resulting mean mechanical interlocking force, also called the anchoring force or simply the mechanical adhesion force [62]. The effective contact area is in either case a key property, as it scales the contribution of friction forces to the resulting anchoring force, according to the relationship in Eq. (3)

$$F_{mechanical} = F_{anchor} = \overline{\mu}\,\overline{P}R \tag{3}$$

where $\overline{\mu}$ is the mean friction coefficient between the coating and the substrate and hence depending on the specific topography, $\overline{P}$ is the mean theoretical pressure needed to keep the coating from sliding off the substrate at a given inclination and R is Wenzel's roughness factor [63].

The relationship between mechanical interlocking force $F_{mechanical}$ and R in Eq. (3) is not new information. In general, the simplest theory of promotion of stability at the coating/steel interface due to roughening of the surface, is explained to be the increase in the surface area available for the formation of primary and secondary bonds, provided that the coating can completely wet the substrate. But the number of bonds formed by mechanical interlocking will also increase, as the equation also states [64,65]. Particularly, it is well established that mechanical interlocking is the primary bonding mechanism for thermally sprayed coatings. Its validity for the stability of organic coatings has however been overlooked and even dismissed for years by the scientific community.

The results presented here show the significant effect mechanical interlocking has on the cathodic disbonding resistance of the polyvinyl butyral/oxide/steel interface. When compensating for the increased effective contact area, the CD resistance was higher on surfaces with features that enabled mechanical interlocking forces. Hence, CD resistance was improved by both increasing effective contact area and mechanical interlocking. Also, water induced adhesion loss improved with mechanical interlocking, as was shown in Fig. 6. The results indicate that CD and wet adhesion depend on the ability of the surface for mechanical interlocking.

Mechanical interlocking will affect the interfacial stability in several ways. It is believed to suppress water accumulation at the interface [66] and total rupture of bonds when accumulation has happened [53] thus increasing the hydrolytic stability of the coating at the interface. A high interfacial stability under humid exposure is suggested to result in higher resistance to lateral ingress of ions from the electrolyte covered defect [51]. This is necessary for a slower CD rate, but also for hydrolytic stability as hydrated cations may contribute to wet de-adhesion
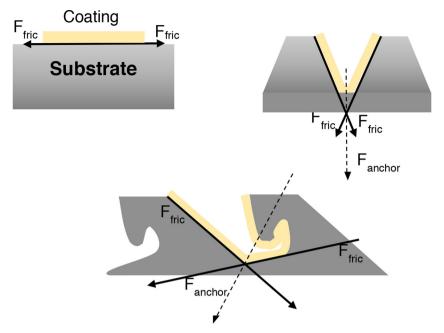
Fig. 9. Sketch of the anchoring force F_{anchor} of a coating as function of the topography of the substrate. Adapted from [62] to explain the anchoring forces in this study.

[67]. The CD progress is believed to proceed by the formation of an area where the coating/substrate interface is affected by the alkaline environment and undergoes structural changes before bonds ultimately fail [38]. Mechanical interactions may stabilize the coating such that coating/substrate bonds are not necessarily broken [42].

Contributions from mechanical interactions have been claimed to make up most of the total adhesion forces at the interface for an organic coating, as mechanical adhesion is expected to be much larger than the adhesion relying on secondary bonding forces that vary with surface oxide chemistry [65,68,69]. Therefore, variations in surface oxide chemistry are not assumed to be responsible for the CD resistance and wet adhesion properties measured. The XPS analysis and surface potentials measured by SKP on bare substrates contribute to this recognition.

Since the mechanical adhesion force scales up with increased effective contact area and interlocking forces the ranking of the surfaces with respect to their ability for mechanical adhesion is: C > B2 > D2 > D1/B1 > A. This ranking mirrors their measured CD resistance.

4. Conclusions

All but the flat A surface allowed for mechanical interlocking. These surfaces had the highest CD rate and highest interfacial ionic mobility. In addition, they suffered from hydrolytic destabilization.

Increasing substrate roughness increased the effective contact area between coating and substrate, and partly explained the improved CD resistance. Features enabling mechanical interlocking forces increased CD resistance even further.

Surface B1 and D1 had similar effective contact area but differed in topography, with more interlocking presumed to be offered by the rectangular peaks on B1. The CD rate was similar on these surfaces. D2 surfaces gave almost twice as much CD as B2 surfaces, even though the tortuosity was only 20% lower. The structures at the bottom of the grooves on B2, probably added to the interlocking of the PVB coating though, which may have increased the CD resistance.

The C surfaces have the highest effective interfacial length, but also the surface with highest ability for mechanical interlocking due to the tilted and curved peaks that can entrap the coating. Little CD and ionic

mobility were found on these surfaces.

Data availability

The raw/processed data required to reproduce these findings cannot be shared at this time as the data also forms part of an ongoing study.

CRediT authorship contribution statement

C.H.M. Hagen: Conceptualization, Methodology, Investigation, Data curation, Writing - original draft. **O.Ø. Knudsen:** Supervision, Writing - review & editing. **A.H. Zavieh:** Writing - review & editing. **W. Pfleging:** Writing - review & editing.

Declaration of Competing Interest

The authors declare that they have no known competing financial interests or personal relationships that could have appeared to influence the work reported in this paper.

Appendix A. Supplementary data

Supplementary material related to this article can be found, in the online version, at doi:https://doi.org/10.1016/j.porgcoat.2020.105766.

References

[1] L.H. Lee, The chemistry and physics of solid adhesion, in: Lee L.H (Ed.), Fundamentals of Adhesion, Plenum Press, London, 1991, pp. 1–86.

[2] C.M.H. Hagen, et al., The effect of surface roughness on corrosion resistance of machined and epoxy coated steel, Prog. Org. Coat. 130 (2019) 17–23.

[3] S.B. Lyon, R. Bingham, D.J. Mills, Advances in corrosion protection by organic coatings: what we know and what we would like to know, Prog. Org. Coat. 102 (2017) 2–7.

[4] A. Leng, H. Streckel, M. Stratmann, The delamination of polymeric coatings from steel. Part 1: calibration of the Kelvin probe and basic delamination mechanism, Corros. Sci. 41 (3) (1998) 547–578.

[5] M. Stratmann, 2005 W.R. Whitney award lecture: corrosion stability of polymer-coated metals - new concepts based on fundamental understanding, Corrosion 61 (12) (2005) 1115–1126.

[6] J.E.O. Mayne, The mechanism of protection by organic coatings, Met. Finish. 12 (143) (1966) 437–441.

[7] P.A. Sørensen, et al., Influence of substrate topography on cathodic delamination of anticorrosive coatings, Prog. Org. Coat. 64 (2–3) (2009) 142–149.

[8] B.C. Rincon Troconis, G.S. Frankel, Effect of roughness and surface topography on adhesion of PVB to AA2024-T3 using the blister test, Surf. Coat. Technol. 236 (0) (2013) 531–539.

[9] D. Ward, An Investigation Into The Effect Of Surface Profile On The Performance Of Coatings In Accelerated Corrosion Tests, Corrosion 2007, NACE, Houston, TX, 2007, p. 16.

[10] J.P.B. van Dam, et al., Effect of surface roughness and chemistry on the adhesion and durability of a steel-epoxy adhesive interface, Int. J. Adhes. Adhes. 96 (2020) 102450.

[11] C.H.M. Hagen, A. Kristoffersen, O.Ø. Knudsen, The effect of surface profile on coating adhesion and corrosion resistance, in: NACE (Ed.), Corrosion 2016, NACE Vancouver, 2016, p. 15.

[12] H.M.C. Hagen, O.Ø. Knudsen, T. Hemmingsen (Ed.), Corrosion Protection of Smooth Surfaces - Coating Adhesion, in Nordic Corrosion Congress, Stavanger, 2015, p. 12.

[13] J.F. Watts, J.E. Castle, The application of X-ray photoelectron spectroscopy to the study of polymer-to-metal adhesion. Part 2 the cathodic disbondment of epoxy coated mild steel, J. Mater. Sci. 19 (1984) 2259–2272.

[14] S.S. Jamali, D.J. Mills, Steel surface preparation prior to painting and its impact on protective performance of organic coating, Prog. Org. Coat. 77 (12, Part B) (2014) 2091–2099.

[15] R.J. Holness, et al., Polyaniline inhibition of corrosion-driven organic coating cathodic delamination on iron, J. Electrochem. Soc. 152 (2) (2005) B73–B81.

[16] N. Wint, et al., The kinetics and mechanism of atmospheric corrosion occurring on tin and iron-tin intermetallic coated steels: I. Cathodic delamination, J. Electrochem. Soc. 162 (14) (2015) C775–C784.

[17] D. Iqbal, et al., Synthesis of ultrathin poly (methyl methacrylate) model coatings bound via organosilanes to zinc and investigation of their delamination kinetics, ACS Appl. Mater. Interfaces 6 (20) (2014) 18112–18121.

[18] G. Williams, H.N. McMurray, Chromate inhibition of corrosion-driven organic coating delamination studied using a scanning Kelvin probe technique, J. Electrochem. Soc. 148 (10) (2001) B377–B385.

[19] G. Williams, H.N. McMurray, Inhibition of corrosion driven delamination on iron by smart-release bentonite cation-exchange pigments studied using a scanning Kelvin probe technique, Prog. Org. Coat. 102 (2017) 18–28.

[20] G. Williams, H.N. McMurray, The mechanism of group (I) chloride initiated filiform corrosion on iron, Electrochem. Commun. 5 (10) (2003) 871–877.

[21] M. Rohwerder, et al., Application of Scanning Kelvin Probe in Corrosion Science, (2005), pp. 605–648.

[22] M. Rohwerder, et al., Application of SKP for in situ monitoring of ion mobility along insulator/insulator interfaces, Electrochim. Acta 54 (25) (2009) 6058–6062.

[23] M. Rohwerder, The Kelvin probe technique as reference electrode for application on thin and ultrathin electrolyte films, in: I. G, L. A, S. F (Eds.), Handbook of Reference Electrodes. Springer, Berlin, 2013.

[24] K. Wapner, M. Stratmann, G. Grundmeier, In situ infrared spectroscopic and scanning Kelvin probe measurements of water and ion transport at polymer/metal interfaces, Electrochim. Acta 51 (16) (2006) 3303–3315.

[25] A. Nazarov, N. Le Bozec, D. Thierry, Assessment of steel corrosion and deadhesion of epoxy barrier paint by scanning Kelvin probe, Prog. Org. Coat. 114 (2018) 123–134.

[26] M. Wicinski, W. Burgstaller, A.W. Hassel, Lateral resolution in scanning Kelvin probe microscopy, Corros. Sci. 104 (2015).

[27] J. Wielant, et al., Cathodic delamination of polyurethane films on oxide covered steel – combined adhesion and interface electrochemical studies, Corros. Sci. 51 (8) (2009) 1664–1670.

[28] R. Posner, et al., Transport processes of hydrated ions at polymer/oxide/metal interfaces: part 1. Transport at interfaces of polymer coated oxide covered iron and zinc substrates, Electrochim. Acta 54 (3) (2009) 891–899.

[29] R. Posner, et al., Transport processes of hydrated ions at polymer/oxide/metal interfaces: part 2. Transport on oxide covered iron and zinc surfaces, Electrochim. Acta 54 (3) (2009) 900–908.

[30] R. Posner, et al., Transport processes of hydrated ions at polymer/oxide/metal interfaces, Electrochim. Acta 54 (3) (2009) 891–899.

[31] B. Salgin, R.F. Hamou, M. Rohwerder, Monitoring surface ion mobility on aluminum oxide: effect of chemical pretreatments, Electrochim. Acta 110 (Supplement C) (2013) 526–533.

[32] ISO 4287, Geometrical Product Specifications (GPS) - Surface Texture: Profile Method -Terms, Definitions and Surface Texture Parameters, International Organization for Standardization, Switzerland, 2000.

[33] ISO 4288, Geometrical Product Specifications (GPS) - Surface Texture : Profile Method – Rules and Procedures for the Assessment of Surface Texture, International Organization for Standardization, Switzerland, 1996.

[34] E. Mottay, et al., Industrial applications of ultrafast laser processing, MRS Bull. 41 (12) (2016) 984–992.

[35] W. Pfleging, A review of laser electrode processing for development and manufacturing of lithium-ion batteries, Nanophotonics 7 (3) (2018) 549.

[36] C.H.M. Hagen, et al., Oxidation of coated steel during exposure to humid air and effects on cathodic disbonding, Electrochimica Acta (2020) submitted for publication.

[37] A. Leng, H. Streckel, M. Stratmann, The delamination of polymeric coatings from steel. Part 2: first stage of delamination, effect of type and concentration of cations on delamination, chemical analysis of the interface, Corros. Sci. 41 (3) (1998) 579–597.

[38] A. Leng, et al., The delamination of polymeric coatings from steel. Part 3: effect of the oxygen partial pressure on the delamination reaction and current distribution at the metal-polymer interface, Corros. Sci. 41 (3) (1999) 599–620.

[39] D.A. Shirley, High-resolution X-Ray photoemission Spectrum of the valence bands of gold, Phys. Rev. B 5 (12) (1972) 4709–4714.

[40] J.F. Moulder, et al., Handbook of X-Ray Photoelectron Spectroscopy, Perkin-Elmer Corp, Physical Electronics Division, Eden Prairie, Minnesota, 1995.

[41] G. Grundmeier, M. Stratmann, Adhesion and de-adhesion mechanisms at polymer/metal interfaces: mechanistic understanding based on in situ studies of buried interfaces, Annu. Rev. Mater. Res. 35 (2005) 571–615.

[42] M. Stratmann, et al., The scanning Kelvin probe; a new technique for the in situ analysis of the delamination of organic coatings, Prog. Org. Coat. 27 (1–4) (1996) 261–267.

[43] L. Lu, et al., The influence of pulse width and energy on temperature field in metal irradiated by ultrashort-pulsed laser, Phys. Procedia 32 (2012) 39–47.

[44] G. Grundmeier, M. Stratmann, Influence of oxygen and argon plasma treatments on the chemical structure and redox state of oxide covered iron, Appl. Surf. Sci. 141 (1) (1999) 43–56.

[45] N. Le Bozec, et al., Influence of stainless steel surface treatment on the oxygen reduction reaction in seawater, Corros. Sci. 43 (4) (2001) 765–786.

[46] J. Wielant, et al., SKP as a tool to study the physicochemical interaction at buried metal–coating interfaces, Surf. Interface Anal. 42 (6-7) (2010) 1005–1009.

[47] A. Nazarov, D. Thierry, Studies in the electrical double layer at Metal/Polymer interfaces by scanning capacitive probe, Prot. Met. 39 (1) (2003) 55–62.

[48] J. Wielant, et al., Influence of the Iron oxide acid − Base properties on the chemisorption of model epoxy compounds studied by XPS, J. Phys. Chem. C 111 (35) (2007) 13177–13184.

[49] A. Nazarov, D. Thierry, Hydrolysis of interfacial bonds in a metal/polymer electrical double layer, Prot. Met. 41 (2) (2005) 105–116.

[50] S.M. Cambier, R. Posner, G.S. Frankel, Coating and interface degradation of coated steel, Part 1: field exposure, Electrochim. Acta 133 (2014) 30–39.

[51] R. Posner, O. Ozcan, G. Grundmeier, Water and ions at Polymer/Metal interfaces, in: M.L.F. Silva, C. Sato (Eds.), Design of Adhesive Joints Under Humid Conditions, Springer Berlin Heidelberg, Berlin, Heidelberg, 2013, pp. 21–52.

[52] W. Fürbeth, M. Stratmann, Scanning Kelvin probe investigations on the delamination of polymeric coatings from metallic surfaces, Prog. Org. Coat. 39 (1) (2000) 23–29.

[53] W. Brockmann, Durability of adhesion between metals and polymers, J. Adhes. 29 (1-4) (1989) 53–61.

[54] H. Leidheiser, W. Funke, Water disbondment and wet adhesion of organic coatings on metals: a review and interpretation, J. Oil Colour Chem. Assoc. 70 (5) (1987) 121–132.

[55] M. Doherty, J.M. Sykes, Micro-cells beneath organic lacquers: a study using scanning Kelvin probe and scanning acoustic microscopy, Corros. Sci. 46 (5) (2004) 1265–1289.

[56] G. Williams, et al., Dopant effects in polyaniline inhibition of corrosion-driven organic coating cathodic delamination on Iron, J. Electrochem. Soc. 153 (10) (2006) B425–B433.

[57] O.Ø. Knudsen, J.I. Skar, Cathodic disbonding of epoxy coatings - effect of test parameters, Corrosion/08, NACE, New Orleans, 2008.

[58] J.I. Skar, U. Steinsmo, Cathodic disbonding of paint films: transport of charge, Corros. Sci. 5 (8) (1993) 1385–1389.

[59] U. Steinsmo, J.I. Skar, Factors influencing the rate of cathodic disbonding of coatings, Corrosion 50 (12) (1994) 934–939.

[60] H. Bi, J. Sykes, An investigation of cathodic oxygen reduction beneath an intact organic coating on mild steel and its relevance to cathodic disbonding, Prog. Org. Coat. 87 (2015) 83–87.

[61] C.F. Glover, et al., Evaluation of multi-layered graphene nano-platelet composite coatings for corrosion control part II – cathodic delamination kinetics, Corros. Sci. 136 (2018) 304–310.

[62] R. Kromer, et al., Laser patterning pretreatment before thermal spraying: a technique to adapt and control the surface topography to thermomechanical loading and materials, J. Therm. Spray Technol. 25 (3) (2016) 401–410.

[63] R. Kromer, et al., Laser surface patterning to enhance adhesion of plasma sprayed coatings, Surf. Coat. Technol. 278 (2015) 171–182.

[64] S.P.M. Noijen, et al., Numerical prediction of failure paths at a roughened metal/polymer interface, Microelectron. Reliab. 49 (9) (2009) 1315–1318.

[65] Ovd. Sluis, S.P.M. Noijen, P.H.M. Timmermans, On the effect of microscopic roughness on macroscopic polymer-metal adhesion, in: W.Dv. Driel, X.J. Fan (Eds.),

Solid State Lighting Reliability: Components to Systems, Springer, 2013.

[66] J.D. Venables, Adhesion and durability of metal-polymer bonds, J. Mater. Sci. 19 (8) (1984) 2431–2453.

[67] M. Kendig, D.J. Mills, An historical perspective on the corrosion protection by paints, Prog. Org. Coat. 102 (2017) 53–59.

[68] A.G. Evans, et al., The fracture energy of bimaterial interfaces, Metall. Trans. A 21 (9) (1990) 2419–2429.

[69] S.P.M. Noijen, et al., A semi-analytic method for crack kinking analysis at isotropic bi-material interfaces, Eng. Fract. Mech. 83 (2012) 8–25.